

An electronic measurement of the Boltzmann constant

This article has been downloaded from IOPscience. Please scroll down to see the full text article.

2011 Metrologia 48 142

(<http://iopscience.iop.org/0026-1394/48/3/008>)

View [the table of contents for this issue](#), or go to the [journal homepage](#) for more

Download details:

IP Address: 132.163.130.139

The article was downloaded on 31/03/2011 at 15:13

Please note that [terms and conditions apply](#).

An electronic measurement of the Boltzmann constant

Samuel P Benz¹, Alessio Pollarolo^{1,2}, Jifeng Qu³, Horst Rogalla^{1,4},
Chiharu Urano^{1,5}, Weston L Tew⁶, Paul D Dresselhaus¹ and D Rod White⁷

¹ National Institute of Standards and Technology (NIST), 325 Broadway, Boulder, CO 80305-3328, USA

² Politecnico di Torino, Corso Duca degli Abruzzi, 24, 10129, Torino, Italy

³ National Institute of Metrology (NIM), Beijing 100013, People's Republic of China

⁴ Department of Applied Physics, Univ. Twente, PO Box 217, 7500 AE Enschede, The Netherlands

⁵ National Institute of Advanced Industrial Science and Technology (AIST), 1-1-1 Umezono, Tsukuba, Ibaraki 305-8563, Japan

⁶ National Institute of Standards and Technology (NIST), 100 Bureau Drive, Gaithersburg, MD 20899, USA

⁷ Measurement Standards Laboratory (MSL), PO Box 31310, Lower Hutt, New Zealand

Received 31 December 2010, in final form 8 February 2011

Published 30 March 2011

Online at stacks.iop.org/Met/48/142

Abstract

The Boltzmann constant k was measured by comparing the Johnson noise of a resistor at the triple point of water with a quantum-based voltage reference signal generated with a superconducting Josephson-junction waveform synthesizer. The measured value of $k = 1.380\,651(17) \times 10^{-23} \text{ J K}^{-1}$ is consistent with the current CODATA value and the combined uncertainties. This is our first measurement of k with this electronic technique, and the first noise-thermometry measurement to achieve a relative combined uncertainty of 12 parts in 10^6 . We describe the most recent improvements to our Johnson-noise thermometer that enabled the statistical uncertainty contribution to be reduced to seven parts in 10^6 , as well as the further reduction of spurious systematic errors and electromagnetic interference effects. The uncertainty budget for this measurement is discussed in detail.

1. Introduction

For ten years, NIST has been developing a Johnson noise thermometer (JNT) with a quantized voltage noise source (QVNS) as a voltage reference. The original goals were to improve thermodynamic temperature measurements through quantum-based electrical measurements and to demonstrate the technique through measurements of the triple point of water and the melting point of gallium [1]. Following these proof-of-principle measurements, higher temperatures were measured at the freezing points of zinc and tin, and showed agreement with archival gas and radiation thermometry measurements [2]. As a result of these measurements and further research and development [3–10], the QVNS-JNT system has evolved through many incremental improvements to the point where a useful measurement of the Boltzmann constant has become practical [11].

The presently accepted value of the Boltzmann constant, $1.380\,650\,4(24) \times 10^{-23} \text{ J K}^{-1}$, is dominated by a single gas-based thermometry measurement with a relative standard uncertainty of 1.7×10^{-6} [12]. There has been much interest in reproducing this measurement, as well as in

methods based on different physical principles that might achieve comparable uncertainty [13]. The QVNS-JNT measurement of the Boltzmann constant is quite different from gas-based measurement techniques, in that it is a purely electronic approach that links the SI kelvin to quantum-based electrical measurements. The QVNS, which is a low-voltage realization of the Josephson arbitrary waveform synthesizer, is programmed to produce multi-tone pseudo-noise voltage waveforms with small ($<1 \mu\text{V}$ peak) amplitudes [10]. The Josephson junctions in the QVNS produce voltage pulses with time-integrated areas perfectly quantized in integer values of $h/2e$, where h is the Planck constant and e is the electron charge. The synthesized voltage is intrinsically accurate because it is exactly determined from the known sequence of pulses, the clock frequency and fundamental physical constants [1, 3]. The QVNS-JNT measurement can, therefore, provide a unique contribution to CODATA analyses of the Boltzmann constant value as well as the planned redefinition of the kelvin [14].

Our QVNS-JNT measurement determines the ratio between the Boltzmann and Planck constants, k/h , by matching the electrical power of a synthetic signal and the

thermally generated noise power of a resistor at the triple point of water [3, 11]. The Johnson noise of a resistor R at a temperature T defines the thermal noise power, which is characterized by its mean square voltage $\langle V_R^2 \rangle = 4kTR\Delta f$, where Δf is the measurement bandwidth [15, 16]. This relation is an approximation to the Nyquist equation and is accurate to a part in 10^6 for frequencies below 10 MHz and temperatures above 250 K. For our measurement of k , we measure the voltage noise of a $100\ \Omega$ resistor at the triple point of water, 273.16 K. The resulting noise voltage has a spectral density of only $1.23\ \text{nV Hz}^{-1/2}$, and must be measured with a low-noise cross-correlation technique [17, 18] in order to extract the resistor signal from the uncorrelated amplifier noise, which has a comparable amplitude and spectral density.

The pseudo-noise-voltage density synthesized by the QVNS waveform, $V_Q = (h/2e)QN_J(Mf_s)^{1/2}$, is determined by defined fundamental constants (h and e), the number of Josephson junctions N_J , the integer number of bits, M , that determine the length of the digital waveform, the clock frequency f_s and a constant Q . Q is the programmable dimensionless fraction of the peak voltage of the Josephson junction and exactly sets the amplitude of the synthesized waveform.

The Boltzmann constant is determined from values of the Planck constant, the triple-point temperature of water, the measured resistance, the QVNS synthesis parameters and the measured ratio of the resistor and QVNS noise-power signals [10, 11]:

$$k = \left(\frac{\langle V_R^2 \rangle}{\langle V_Q^2 \rangle} \right)_f \frac{h Q^2 N_J^2 f_s M}{16 T X_R}, \quad (1)$$

where X_R is the measured resistance expressed in units of the von Klitzing resistance $R_K \equiv h/e^2$. The cross-correlated electrical and thermal noise powers are compared over discrete frequency intervals centered at the frequency of the harmonic tones of the synthesized waveform [10], a process that will be described below in more detail. Since the relative standard uncertainty for the Planck constant is about two orders of magnitude smaller than that for the Boltzmann constant, we use the 2006 CODATA value, $h = 6.626\ 068\ 96(33) \times 10^{-34}\ \text{J s}$ [12], to determine our value of the Boltzmann constant.

2. Experimental apparatus

The circuit schematic in figure 1 shows the two channels (A and B) of the correlator that simultaneously measure one of the two voltage sources. The switching network alternates or ‘chops’ between the two input signals at 100 s intervals, such that both channels simultaneously measure either the resistor noise or the QVNS voltage signals. This technique minimizes the effects of time-dependent variations in the response of the cross-correlation electronics. Each channel consists of a series of amplifiers and filters, followed by an analogue-to-digital converter (ADC). The digitized signals from each channel are optically transmitted to the computer, where software computes and averages the auto- and cross-correlation spectra of many ‘chops’.

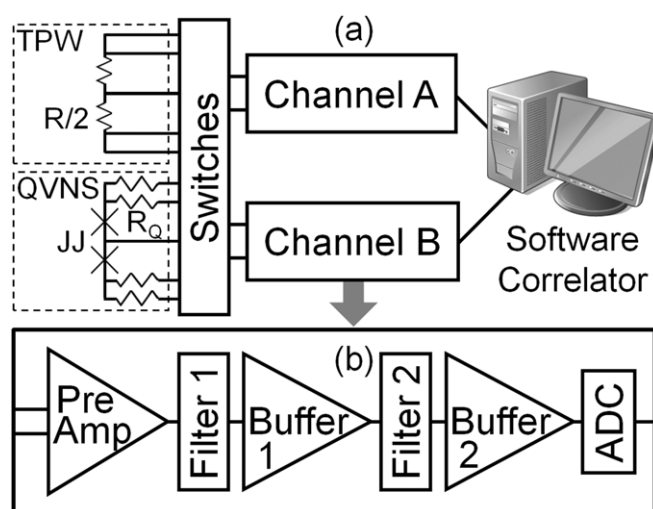


Figure 1. Schematic of the two-channel QVNS-JNT cross-correlation electronics, showing (a) the output wiring of the triple point of water (TPW) and QVNS probes (where the fifth wire is ground), and (b) the specific components of each channel, including the differential input leads to the preamplifier and the optical interface between the analogue-to-digital converter (ADC) and the computer that performs the correlation analysis.

The design of the resistor and QVNS circuits are described elsewhere in detail [1, 2, 10]. The value of the on-chip resistor in each QVNS output lead, R_Q , is equal to the total sense resistor value, R . The signals from both sources are connected to each preamplifier via a differential twisted pair of leads and a fifth shield wire that defines ground potential. The resistor circuit is a custom Ni–Cr-alloy foil on an alumina substrate mounted in a hermetically sealed package. The resistor sensor package is mounted on a beryllia header in a custom-made probe designed to reduce thermal errors when inserted into the triple-point-of-water cell. The triple-point cell environment is maintained near $0.01\ ^\circ\text{C}$ with a thermoelectric cooler.

The QVNS chip is a niobium superconducting integrated circuit fabricated at NIST in Boulder, and has a total of eight Josephson junctions [10]. The chip is mounted on a microwave-compatible flexible cryopackage within a magnetically shielded cryoprobe, which is cooled to 4 K in a 1001 liquid helium storage dewar. The QVNS circuit and lead resistors R_Q are maintained at 4 K.

The impedances of the transmission lines, which transmit the voltage signals between the preamplifier in a given channel and each source, are carefully matched in order to maximize the measurement bandwidth and minimize frequency-dependent correction terms in the analysis [3]. Lossy ferrite beads are used on the differential leads at the amplifier input to suppress Colpitts oscillations at frequencies above 10 MHz that can arise between the JFETs when the amplifiers of the different channels are connected in parallel through the measurement circuit. Without the ferrites, these oscillations between the JFET differential input stages, which have a bandwidth of 50 MHz, are of sufficient amplitude to drive the amplifiers into saturation.

Each high-performance JFET preamplifier has low input noise voltage ($\sim 0.85\ \text{nV Hz}^{-1/2}$), high gain ($\sim 3160\times$ or

70 dB), high linearity and high common-mode rejection (~ 100 dB at 100 kHz), over the full measurement bandwidth. The preamplifier also operates without feedback around the JFET input stage in order to prevent errors from correlations between the input noise voltage and the input noise current [19]. In addition, the preamplifier also provides a high input resistance to minimize the load on the resistor noise source. A significant portion of the research and development of the QVNS-JNT system has entailed optimizing the preamplifier and improving these features, especially the linearity [5–9].

Two passive low-pass filters, and corresponding buffer amplifiers, each with $11\times$ gain, are used in each channel [8–9]. Both filters have 11 poles, but have different cutoff frequencies of 650 kHz and 800 kHz. This large effective number of poles is necessary to maximize the measurement bandwidth and ensure that aliased signals from the ADCs are at least 120 dB lower than the ‘in-band’ signals for frequencies up to 650 kHz. This steep amplitude reduction prevents the aliased high-frequency signals of each channel from adding to the measurement of the in-band signals.

The ADCs sample the voltage signals for nearly 1 s with 2^{21} samples at a rate of 2.083 MHz (50 MHz clock for 24 bits, of which only 16 are used for data [9]). This produces frequency-resolved bins of 0.9934 Hz and a 1.042 MHz Nyquist frequency that defines the ADC bandwidth. The 1 s data sequences from both channels are optically transmitted to the digital receiver card in the computer, which computes the fast-Fourier transform (FFT) of the sequences and calculates the autocorrelation for each channel and the cross-correlation between the channels. The receiver accumulates and averages 100 of the 1 s FFTs for each ‘chop’, and stores the two real and one complex frequency-domain data arrays on the computer. The switching network then ‘chops’ the correlator input to the alternate source for the next measurement.

The QVNS-synthesized pseudo-noise voltage spectral density is set to exactly $V_Q \equiv 1.228\,000\text{ nV Hz}^{-1/2}$, which closely matches the noise voltage spectral density $V_R = 1.228\,263\text{ nV Hz}^{-1/2}$ of the $100.0051\ \Omega$ resistor at the triple point of water. The QVNS pseudo-noise waveforms consist of a ‘comb’ of harmonic tones that are equally spaced in frequency (typically odd consecutive tones) and have identical amplitudes and random relative phases [4, 10]. The spacing of the harmonic tones Δf_h is determined by the code length and the choice of harmonics.

Data presented in this paper are from two different QVNS waveforms that both consist of odd harmonic tones, but have different code lengths, $M = 3 \times 2^{23}$ (~ 25 Mb) and 3×2^{26} (~ 200 Mb), and correspondingly different tone spacings ($\Delta f_h = 2f_s/M$) of 794.73 Hz (25 Mb) and 99.34 Hz (200 Mb). Because the codes’ lengths differ by a factor of eight, the rms voltage amplitude of the synthesized tones is also different for each waveform, 34.618 46 nV (25 Mb) and 12.239 48 nV (200 Mb). Although the code lengths, tone densities and tone amplitudes are different for the two waveforms (requiring them to have different values of Q), the total voltage noise, V_Q , and the average voltage spectral density of each waveform remain the same.

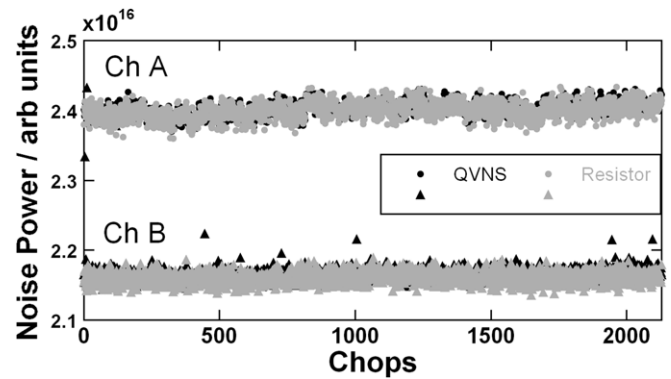


Figure 2. Auto-correlated resistor and QVNS signals of both channels for the 1.589 kHz bin (794.73 Hz wide) from data set 1 versus the chop number (consecutive 100 s intervals). Eight chops of the channel B QVNS measurements indicate an overload event.

3. Experimental results

Below we present the results from the analyses of two different data sets, taken 3 months apart, each with a total acquisition time of 116.6 h. The first, data set 1, used the shorter 25 Mb-length QVNS waveform, while the second, data set 2, used the 200 Mb waveform. Measurements of both of these data sets benefited from several recent improvements to the experiment. One of the improvements was the use of mu-metal shielding around the electronics to reduce electromagnetic interference (EMI) [9]. Some EMI signals were found to cause the preamplifiers to occasionally overload, which necessitated the removal of some chop sequences from the analysis.

Newer improvements, which also helped reduce ‘EMI-induced amplifier overloads,’ include better management of ground connections with a low-resistance connection to a newly installed earth point, elimination of ground loops, and dedicated mains power lines and conduits. Figure 2 shows how the intermittent larger autocorrelation amplitudes of individual chop measurements corrupted by overload signals were found in data set 1 by characterizing an individual frequency bin over many chops [9]. The improvements sufficiently reduced the EMI, such that the resistor measurements showed no overloads (compared with [9]) and QVNS measurements showed only occasional overloads in channel B. These remaining overloaded chops were removed in the software analysis by eliminating those eight ‘chops’ and the corresponding resistor chops from the accumulated data.

Increased linearity of the preamplifiers was another improvement. This was achieved through the addition of an active circuit that nulls the dc offset at the output of the post-amplification stage of each preamplifier. In previous measurements, the dc offsets for the different preamplifiers were found to be directly proportional to the measured amplifier non-linearity [8]. This is consistent with the imperfect matching of operating points of the transistors in the differential input stage, which leads to an offset accompanied by incomplete cancellation of the even-order distortion effects. As a result of the improved preamplifier linearity, the dominant

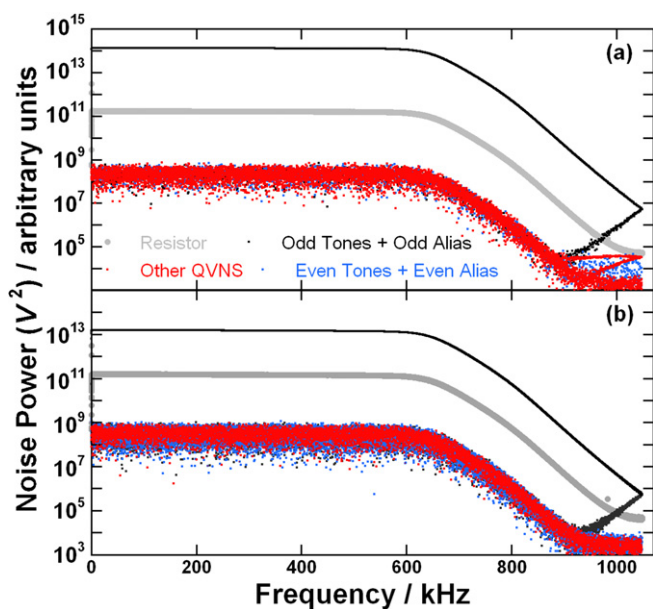


Figure 3. Cross-correlated measured noise-power signals for data sets (a) 1 (794 Hz tone spacing) and (b) 2 (99 Hz spacing), showing the QVNS-synthesized comb waveform (black and red) and the resistor noise (grey). The black points represent the QVNS comb tones, while the red points show the noise floor after averaging for 116.6 h (2098 chops of 100 s per chop for each source) for both data sets.

(This figure is in colour only in the electronic version)

non-linearity in the measurements now appears to occur in the ADC circuit and its on-board amplifier [8].

For both data sets, the cross-correlation electronics are powered with Li-ion batteries. However, we have not implemented continuous recharging because the measured statistical uncertainty increases intermittently for some chop measurements. This appears to be similar to the EMI-induced amplifier overloads, but it is a more subtle and difficult effect to detect and eliminate. Therefore, the data presented in this paper have electronics that are powered with isolated Li-ion batteries. The batteries are recharged during the day and the data are collected overnight.

The averaged cross spectra for the signals from both the QVNS and resistor sources for both data sets are shown in figure 3. The data show the frequency response of the measurement system, and in particular the combined transfer function of the filters, which dramatically decrease the signals for frequencies above 650 kHz (by seven decades at 1 MHz). There are a number of important features that can be seen from these data. The FFTs of the resistor signals for the two data sets are similar, but the amplitudes of the QVNS harmonic tones differ by eight-fold for the two data sets and differ from the resistor power by their respective tone spacing Δf_h . As a result of averaging the cross-correlated signals over many samples, the *uncorrelated* noise floors of both QVNS spectra are more than two orders of magnitude below those of the *correlated* resistor noise powers, even though the resistor and preamplifier noise powers are of comparable value. Note that the QVNS harmonic tones at frequencies above the Nyquist frequency are aliased back to lower frequencies not coincident

with the lower frequency tones, while the aliased resistor noise signals are combined with the non-aliased signals in root-sum-square (RSS) fashion to produce larger rms amplitudes.

One of the more distinct differences in the spectra is the absence in figure 3(b) of second-harmonic distortion of the QVNS tones (blue even-tone data points including their aliases), which is noticeable in figure 3(a) at frequencies above 850 kHz. Experimental investigations suggest that this distortion is due to non-linearities in the ADC circuit (as mentioned above and in [8]). It is not visible in the data of figure 3(b), because the same total second-harmonic-distortion power is distributed as 64 times the number of distortion products of 1/64 the amplitude, with random phases, across 8 times as many FFT bins, with amplitudes an average of 27 dB (a factor of $8\sqrt{8}$) below those of figure 3(a).

Another feature that is different for the two data sets is that spurious signals and their aliases can be seen above 880 kHz in figure 3(a). The source of these signals was found to be an oscillation in the ADC voltage regulators, which seems to have mixed with the QVNS tones. The source of the oscillation was eliminated and these undesirable signals do not appear in the spectra of data set 2.

Two additional changes produced minor differences in the frequency responses of both channels for the two data sets. First, the frequency response of the transmission lines for data set 2 had more attenuation in the measurement band than for data set 1, because ferrite beads of different materials were used at the four preamplifier inputs. Second, while adding the automatic output voltage compensation circuit to the last stage of the differential amplifiers of the preamplifier circuit, a resistor was accidentally left open-circuit and slightly changed the amplification of the non-inverting part of the differential amplifier. This happened in the preamplifiers of both channels prior to the measurements of data set 1. As a result, the preamplifiers had a reduced common-mode rejection, so the JNT system was more sensitive to EMI. This problem was discovered and repaired prior to the measurements of data set 2. Note that all chops of data set 2 were entirely free of EMI-induced overloads of the preamplifiers, and this appears to be due to the elimination of ground loops.

Some of the features described above are also shown in figure 4, which plots the power spectra (calculated as the autocorrelation), rather than the cross spectra, of the measured noise power for each channel for both data sets. In order to directly compare them on a similar vertical axis, the noise powers of both data sets are summed (or ‘rebinned’) over the same 794 Hz frequency intervals, which is the frequency spacing of data set 1. The difference between the noise powers of each data set is shown in figure 4(b) for both channels. The higher sensitivity to external noise for data set 1 is visible in both the noise power and difference data, which show larger power from EMI signals at a few frequencies. The low-frequency noise power for data set 2 is about 9% lower than that of data set 1, largely the result of the gain shift from the open-circuit resistors. The frequency-dependent difference between the noise powers is clearly not quadratic, which suggests that the response is a combination of impedance-matching differences due to the lower-impedance ferrites for

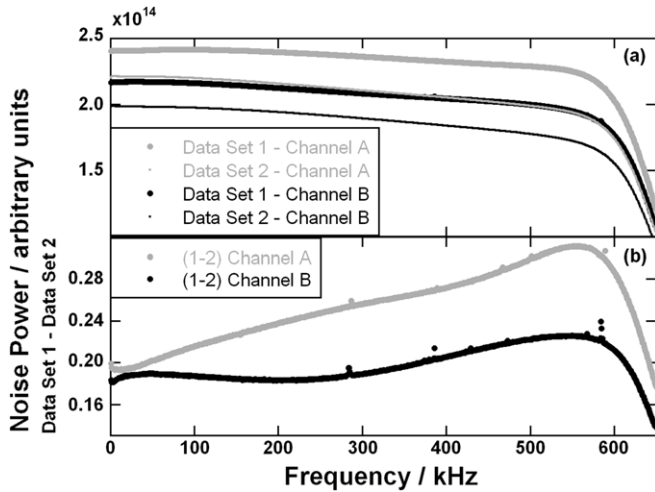


Figure 4. Frequency response of the measured noise power signals for data sets 1 and 2 showing (a) the autocorrelation of each channel and (b) the difference between each channel.

data set 1 and sensitivity to the common-mode noise signals from both sensors. Unfortunately, we did not characterize the common-mode rejection ratio (CMRR) of the open-circuit resistor circuit for data set 1, so this supposition was not confirmed.

After measuring a large number (2098 chops) of cross-correlated power spectra for each data set, we average all the data and calculate the noise power over frequency intervals of the harmonic tone spacing Δf_h (the effective resolution bandwidth), where the center frequency of these ‘rebinned’ data is at the frequency of each odd harmonic tone [3]. The ratio of the real parts of both the thermal and QVNS noise power is calculated for each of these frequencies. Then, a two-parameter, least-squares fit, $a_0 + a_2 f^2$, is used to analyse these ratios over the 650 kHz measurement bandwidth. Fitting the data in this way removes any remaining frequency-dependent differences between the electronic and thermal noise power [9] that result from small differences in the time constants due to imperfect impedance matching. The resulting fitting coefficients, a_0 and a_2 , and the relative standard uncertainty for each coefficient are important characteristics of the data.

Figure 5 shows the residuals of the fitted ratios for both data sets. Because of its smaller frequency range Δf_h , data set 2 has eight times more points than data set 1, and the residuals have a correspondingly larger variance. The plot shows that the amplitudes of the residuals of both data sets have negligible frequency dependence over the measurement bandwidth up to the 650 kHz cutoff frequency of the first filter. In fact, these are the ‘flattest’ residuals we have measured with respect to all previous measurements. This flatter frequency response of the electronics is a result of many improvements, but in particular, improved amplifier linearity and the reduced aliased signals due to the larger number of filter poles.

For the measurement of the Boltzmann constant, we are interested primarily in the coefficients produced from fitting the data over a 640 kHz measurement bandwidth (Δf_m) from 10 kHz to 650 kHz (precise values are 9.934 kHz to 649.691 kHz, and $\Delta f_m = 639.757$ kHz). The maximum

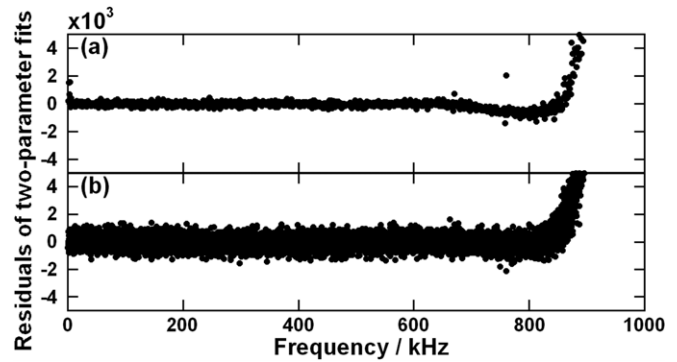


Figure 5. Frequency response of the ratio of the thermal and QVNS cross-correlated noise powers after least-squares fitting over the 10 kHz to 650 kHz frequency range: residuals of (a) data set 1 and (b) data set 2. Each data set was averaged for over 116.6 h, which corresponds to 2098 chops of 100 s each for each source.

frequency was chosen to match the cutoff frequency of filter 1. The low-frequency starting bin was chosen to avoid frequencies below 10 kHz, which had been susceptible to overload effects. When overloads are not present, then the low-frequency starting point is typically reduced to 2 kHz, which is above the 1 kHz high-pass cutoff frequency of the preamplifiers and avoids the difficult-to-shield low-frequency harmonics of the mains supply.

In order to explore the self-consistency of the data, especially the quadratic response, we also analysed the data over successively smaller bandwidths, with different maximum frequencies. Figure 6(a) shows the difference of the constant ‘offset’ coefficient a_0 from the calculated value $a_0^{2006} = 4kTR/(1.228\,000 \times 10^{-9})^2 = 1.000\,428\,54$, which is based on the 2006 CODATA value of k . The difference expression $a_0 - a_0^{2006}$ is equivalent to the relative difference $(k - k_{2006})/k_{2006}$, which is used below, as well as the relative temperature differences $(T - T_{90})/T_{90}$, which we presented in previous publications. The statistical uncertainty at each bandwidth is based on the standard error estimates for a_0 from that fit.

Figures 6(b) and (c) show the bandwidth dependence of the second-order coefficients for the two data sets. Compared with a_0 , the a_2 coefficients are one order of magnitude smaller for data set 1 and two orders of magnitude smaller for data set 2. These small second-order coefficients demonstrate that the resistor and QVNS transmission lines are well matched, especially for the measurements of data set 2, and that there is no significant quadratic component to the ratio measurement.

For all of these ratio measurements, a quadratic fit was used to determine the noise power ratio and remove any remaining frequency-dependent differences between the electronic and thermal noise power [2, 3], which result from small differences in the time constants due to imperfect impedance matching. The offset coefficients for the four largest bandwidth calculations are in excellent agreement for the two data sets, which would suggest confidence for the full-bandwidth calculations. However, for the smaller-bandwidth calculations, the offsets for the two data sets are in greater disagreement, and the offset for data set 2 is much larger than for the larger-bandwidth calculations. Another interesting

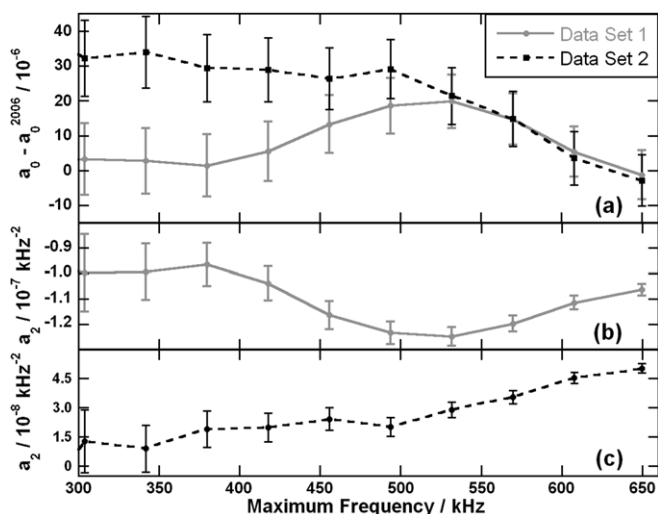


Figure 6. Quadratic fit coefficients for both data sets determined by fitting the data over different maximum frequencies: (a) a_0 difference from 2006 constants and a_2 for data sets (b) 1 and (c) 2. Connecting lines show the trends. The starting frequency for all the fits was 10 kHz.

feature is that the a_2 coefficients for each data set appear to have an inverse frequency response with respect to that of a_0 . These unusual features may be real effects of the measurement, such as possible common-mode signals, for example, or they may be artifacts of our fitting procedure. Additional measurements and analysis will be required to understand these features. We include these effects as a type B uncertainty in the following uncertainty analysis.

Finally, in figure 7 we present change in the constant offset coefficient a_0 for each data set, including the value found from averaging the data from *all* chops, as well as values determined from smaller data sets that were measured on different days. The offset coefficients were determined by fitting the data up to the 650 kHz maximum frequency. An interesting point, which is not shown in figure 7, is that the coefficients of data set 2 were not substantially changed when the low-frequency starting bin was reduced from 9.934 kHz to 1.986 kHz. However, the coefficients of data set 1 changed significantly, indicating that this data set contained additional chops (that were not manually removed like the largest ones) that are possibly corrupted by EMI.

4. Uncertainty analysis

The uncertainties are divided into four main categories that correspond to specific factors in equation (1). These are the measured spectral power ratio (SPR), $\langle V_R^2 \rangle / \langle V_Q^2 \rangle$; the measured resistance $R = X_R R_K$; the realization of the water triple-point temperature T_{WTP} and the QVNS reference waveform scaling factor Q . The tabulated uncertainties shown in all the tables are stated as standard relative uncertainties, $u_r(x) \equiv u(x)/x$. The uncertainty $u_r(\text{SPR})$ associated with the measurement of the spectral power ratio is by far the dominant uncertainty. Other factors in equation (1), such as those associated with the sampling frequency and the Planck constant, have negligible uncertainty.

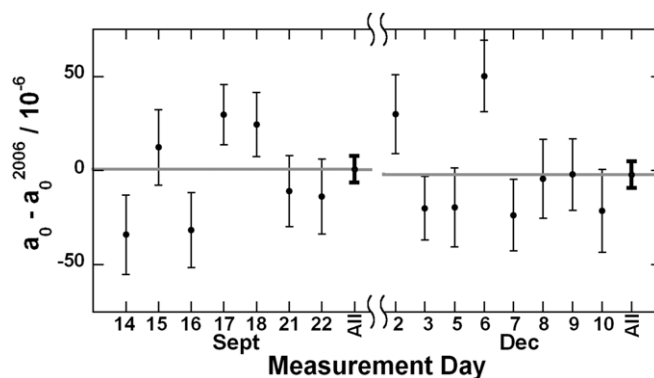


Figure 7. Difference of the constant ‘offset’ coefficient a_0 from the calculated value a_0^{2006} determined from both complete data sets (*All*), and for smaller data sets (with fewer chops and shorter periods ranging from 14 h to 24 h each) collected on different days. Error bars represent the standard relative uncertainty, and the fits were determined over the 10 kHz to 650 kHz frequency range.

Table 1. Difference in the constant ‘offset’ coefficient a_0 from the calculated value a_0^{2006} for each data set (fit over 10 kHz to 650 kHz) and for the combined data, including the standard uncertainty.

Data set	$(a_0 - a_0^{2006}) \times 10^{-6}$	$u_s(a_0)$
1	2.25	7.40
2	-1.09	7.36
Combined	0.57	5.22

4.1. Spectral power ratio

Noise statistics and combined results. The spectral power ratio was determined for each data set in the low-frequency limit via the fit parameter a_0 . A simple quadratic frequency correction accounts for the degree to which the impedances of the R probe and QVNS probe remain slightly unmatched. The least-squares two-parameter fit implements the correction model to determine both a_0 and the small quadratic coefficient a_2 . The relative statistical uncertainty $u_s(a_0)$ is essentially a measure of the magnitude of the random variations remaining in the cross spectra for the available averaging period t_a (116.6 h for each data set) [4]. As a statistic, $u_s(a_0)$ is proportional to the standard deviation in the mean for the entire measurement bandwidth of $\Delta f_m = 640$ kHz and is proportional to $(\Delta f_m t_a)^{-1/2}$. Values of $u_s(a_0)$ for the two data sets are given in table 1 and are combined as statistically independent uncertainty estimates.

The values of a_0 for the two data sets are combined as a weighted average of the two results. The combined weighted average value for a_0 and combined uncertainty $u_s(a_0)$ are shown in the bottom row of table 1. The statistical uncertainty for the combined data is also given in table 2.

Correction model. The correction model assumes a pure quadratic frequency dependence in the ratio spectrum, and this has a strong physical basis. The leading term in all approximations of the ac characteristics of both the transmission lines and the preamplifier noise will be quadratic [19]. When approaching uncertainties on the order of 1×10^{-6} , however, other forms of frequency dependence need to be

Table 2. The principal standard uncertainties for the measurement of the spectral power ratio.

	$u_r/10^{-6}$
Statistics	5.2
Correction model	2.0
Spectral aberrations	10.4
EMI	2.0
Distortion	1.0
$u_r(\text{SPR})$	12.0

considered. The most important of these is a linear frequency term a_1 that would be expected due to dielectric loss in any insulators forming shunt admittances of the input circuits [20]. There is no practical way, however, to evaluate such small linear terms in the spectra via simple least-squares statistics alone, due to the magnitude of the remaining correlated noise. In practice, only the quadratic term can be evaluated via statistical fitting for the noise data presented here.

Instead, we estimate the value of a_1 from knowledge of the typical admittances associated with the preamplifier input circuits [2]. The most likely origin of dielectric losses are those originating in the printed-circuit-board traces for the relays of our switch card made from FR4 composite insulator material [21]. There are three linear frequency terms that arise as each of the two probes couples differently to the input circuit capacitance, producing both filtering terms and a correlated noise term. The two filtering terms associated with the dielectric loss nearly cancel due to the balancing of series termination resistors R_Q in the QVNS probe with the differential resistance R of the resistor probe according to $R_Q \cong R$ (see figure 1). This leaves one remaining linear frequency term that cannot be balanced, because it exists only when coupling to the resistor probe and not to the QVNS probe. This leads to a correlated dielectric-noise term from the FR4 given by

$$a_1 \cong 2\pi \frac{T_{\text{FR4}}}{T_{\text{WTP}}} R C_{\text{FR4}} \tan \delta_{\text{FR4}}, \quad (2)$$

where C_{FR4} , $\tan \delta_{\text{FR4}}$ and T_{FR4} are the shunt capacitance, loss tangent and temperature of the circuit board material, respectively. Given $C_{\text{FR4}} \tan \delta_{\text{FR4}} \lesssim 0.04$ pF, and $T_{\text{FR4}} \cong 296$ K, with a rectangular probability distribution, we estimate a value of $a_1 \cong 8 \times 10^{-9}$ kHz $^{-1}$. When noise data are simulated with this *a priori* value for a_1 and reasonable values for a_2 are included, errors in a_0 of about 2×10^{-6} are predicted.

Spectral aberrations. The transmission lines of the resistor and QVNS probes are tuned to produce a ratio spectrum that is as flat as practical, and the remaining quadratic term in the frequency response is accounted for through fitting. Despite these efforts, the fit residuals are not perfectly flat within the measurement band, and small but broad spectral aberrations remain. These features are aberrations in the sense that they are not consistent with simple filtering effects and evidently have a more complex origin. Both data sets exhibit spectral aberrations of somewhat different character over the first few hundred kilohertz, the net effect of which is a dependence of a_0 on the upper frequency limit of the fit, as shown in figure 6(a).

The two data sets yield consistent values for a_0 for fitting limits above 525 kHz. Our highest fit limit of 650 kHz is set by the existence of the higher-order frequency dependence, which becomes dominant above that limit. For the region between 525 kHz and 650 kHz, however, there remains a noticeable fit limit dependence, which we interpret as the effect of the aberrations. The fitted value for a_0 changes by approximately 18×10^{-6} over this frequency limit interval. At present, we cannot model or otherwise explicitly correct for this effect, and the simple quadratic fitting process essentially averages over the aberrant regions. We account for this ambiguity by assigning a rectangular probability distribution of half-width 18×10^{-6} , which yields a standard uncertainty of approximately 10.4×10^{-6} to account for the existence of spectral aberrations.

Electromagnetic interference. EMI is another unavoidable source of error. It is typically intermittent, caused by nearby electrical machinery not associated with the JNT, and any magnetically-coupled EMI is difficult to shield at low frequencies. To minimize possible EMI effects, all of the analogue electronics and the ADCs are operated from independent battery power supplies, and the ADCs are coupled to the computer via fiber-optic links. As described above and elsewhere [9], EMI of sufficiently large amplitude was found to overdrive the amplifiers, which produced distortion and frequency-dependent errors. Additional shielding and careful grounding reduced these overloads, and measurement analysis allowed us to detect chops containing transient overloads so they could be removed from the final data analysis. However, EMI signals with amplitudes that are small relative to the measured signals, especially those below the amplifier noise, are more difficult to detect. This is most problematic in measurements of the resistor signal where the white noise spectrum masks possible small interferences at all frequencies. While statistical tests on the averaged power spectra can detect stationary single-frequency EMI, in general the tests are not sufficiently powerful to detect all types of EMI [22].

Evidence of the absence of EMI effects in the noise ratio measurements was obtained by separate tests of the QVNS and resistor circuits, configured such that the two circuits would ideally generate no correlated signals [22]. The QVNS was operated to generate zero volts (zero output from the code generator) and the sense resistor circuit was modified by connecting two of the differential leads to ‘dummy’ series resistors of the same 50 Ω impedance and geometric layout as the real sensor [23]. When these modified null correlated-noise sources were measured with the JNT electronics, the resulting cross-correlated signals decreased with increasing integration period (more chops) as the uncorrelated noise from their lead resistances gradually decreased. Any remaining non-zero noise-power would then indicate a potential corruption from EMI. After a full day of integration, these tests yielded residual correlated-noise powers of relative magnitude 0.1 $\mu\text{W W}^{-1}$ and 0.3 $\mu\text{W W}^{-1}$ in the QVNS and resistor probes, respectively. These tests, however, were performed well after the completion of the second data set, when certain circuit configurations had been changed in the electronics. Hence, we were not able to

exactly emulate the same experimental conditions that existed during the time when the data were obtained and we cannot rule out the possibility that the susceptibility to EMI was greater during the earlier data sets.

As was discussed in section 3, there were several indications that both the susceptibility to EMI and the presence of EMI were higher in data set 1 than that of data set 2. We therefore chose to use the difference between the results of the two data sets, $a_0(1)$ and $a_0(2)$, to set an estimated upper bound on the magnitude of possible EMI corruption in the ratio spectra. Specifically, using the results shown in table 1, $u_r(\text{SPR}_{\text{EMI}}) \approx (a_0(1) - a_0(2))/3^{1/2} \approx 1.9 \times 10^{-6}$ for an assumed rectangular probability distribution. This estimate, which is far more conservative than the results of the EMI null tests would suggest, reflects the difficulty in accounting for the effects of transient EMI. For the purposes of the SPR uncertainty budget shown in table 2, we round the estimate up to $2 \mu\text{W W}^{-1}$.

Distortion. Distortion products due to any non-linearity in the correlator lead to errors in the noise-power measurement, and hence in the measured spectral power ratios. The distortion in each channel can be modeled as

$$V_{\text{out},i} = \sum_{j=0}^{\infty} a_{i,j} (V_{\text{in},i} + V_{n,i})^j, \quad (3)$$

where $V_{\text{in},i}$ and $V_{\text{out},i}$ are, respectively, the input and output voltages, and $V_{n,i}$ are the equivalent input noise voltage for each amplifier channel and the linear terms $a_{1,1}$ and $a_{2,1}$ are assigned a value of 1.0. If only the most significant terms are considered, then the measured spectral power ratios, calculated from the product of the two output voltages, have the expected value

$$\frac{\langle V_Q^2 \rangle}{\langle V_R^2 \rangle} \Big|_{\text{meas}} = \frac{\langle V_Q^2 \rangle}{\langle V_R^2 \rangle} \left(1 + 3 \left(\frac{a_{1,3}}{a_{2,1}} + \frac{a_{2,3}}{a_{1,1}} \right) (\langle V_Q^2 \rangle - \langle V_R^2 \rangle) + 3 \frac{a_{1,3}}{a_{2,1}} (\langle V_{n,1,Q}^2 \rangle - \langle V_{n,1,R}^2 \rangle) + 3 \frac{a_{2,3}}{a_{1,1}} (\langle V_{n,2,Q}^2 \rangle - \langle V_{n,2,R}^2 \rangle) - \langle V_{n,2,R}^2 \rangle + \frac{a_{1,2} a_{2,2}}{a_{1,1} a_{2,1}} \left[3 (\langle V_Q^2 \rangle - \langle V_R^2 \rangle) + (\langle V_{n,1,Q}^2 \rangle - \langle V_{n,1,R}^2 \rangle) + (\langle V_{n,2,Q}^2 \rangle - \langle V_{n,2,R}^2 \rangle) + \frac{\langle V_{n,1,Q}^2 \rangle \langle V_{n,2,Q}^2 \rangle}{\langle V_Q^2 \rangle} - \frac{\langle V_{n,1,R}^2 \rangle \langle V_{n,2,R}^2 \rangle}{\langle V_R^2 \rangle} \right] \right), \quad (4)$$

where the equivalent input noise powers are given the additional subscript Q or R to indicate the noise source being measured. This source distinction is important, because the attributed uncorrelated noise in each channel must include the thermal noise generated by the lead wires of the respective connections to the preamplifiers. Equation (4) shows that if the various noise sources are matched according to $\langle V_Q^2 \rangle = \langle V_R^2 \rangle$, $\langle V_{n,1,Q}^2 \rangle = \langle V_{n,1,R}^2 \rangle$ and $\langle V_{n,2,Q}^2 \rangle = \langle V_{n,2,R}^2 \rangle$, then the error in

the measured spectral power ratio, due to distortion effects, is zero. This is the rationale for the close matching of the QVNS and R noise sources as described in section 2.

An important feature of equation (3), unlike previous distortion analyses (e.g. [4, 23]), is that it includes the second-order distortion coefficients $a_{1,2}$ and $a_{2,2}$. These terms have been neglected in earlier analyses because they appear in equation (3) as the product of two small terms, and were therefore expected to be negligible. However, measurements using a two-tone test showed that the second-order distortion is, in fact, dominant [6, 8]. The reduction of second-order distortion was also the rationale for the auto-offset-null circuits described in section 3. All of the relative error terms included in equation (4) scale as voltage squared.

Measurements at 300 kHz of two-tone waveforms, made at several different amplitudes, and then extrapolated to the typical input voltage for the correlator, show that both the second- and third-order terms, respectively, contribute errors of only 2×10^{-5} and 3×10^{-6} in the power spectral ratio at 300 kHz, without considering the additional benefits of matching the noise powers. However, this simple analysis neglects the potential frequency dependence of the non-linearities. Frequency dependence may arise because non-linearities can be reduced by negative feedback, with the consequence that second- and third-order distortion terms of equation (4) rise as frequency squared and cubed as the loop gain of the amplifier falls away. In the correlator, the frequency dependence of at least some of the contributions to the second-order distortion products will therefore increase as frequency to the fourth power. When the frequency dependence is considered, such distortion effects become increasingly significant as the 650 kHz upper cutoff frequency of the correlator is approached. The greatest contribution at 650 kHz is due to the second-order distortion, but can be offset by matching the QVNS and R noise powers to better than about 0.1%, and the uncorrelated noise power in each channel to within 0.2%. The match in the QVNS and R powers is easily achieved by the appropriate choice of the factor Q in equation (1), as already discussed. The match in the uncorrelated noise sources, or more specifically the leadwires to the preamplifiers, is achieved by the insertion of small ($< 1 \Omega$) resistors. We assign a standard uncertainty of 1×10^{-6} to account for any remaining unmatched distortion effects.

The combined uncertainty $u_r(\text{SPR})$ for the spectral power ratio is the RSS of the individual uncertainty components shown in table 2.

4.2. Resistance measurement

The resistance was measured periodically between noise data acquisition cycles. A simple bipolar dc method was used to compare voltages across the two-terminal-pair junctions of the resistor-probe resistance with the analogous voltages from a calibrated 100Ω reference resistor. Excitation currents of $\pm 500 \mu\text{A}$ were used for most measurements, and checks for power dependence indicated no observable effects. The statistical relative uncertainty was typically 0.4×10^{-6} for a series of 250 individual measurements.

The reference resistor is a 100 Ω hermetic encapsulated type with a calibration history traceable to the as-maintained ohm via the quantum Hall effect (QHE) at NIST [24]. The use of the QHE to maintain the ohm is the standard approach [25] worldwide to assure the highest uniformity and stability in the disseminated unit by adopting the conventional value for the von Klitzing constant $R_{K-90} \equiv 25\,812.807\ \Omega$. This as-maintained value is judged to be consistent with the SI ohm with an uncertainty of only 0.02×10^{-6} . The drift rate of the reference resistor has been determined to be $0.05\ \mu\Omega/(\Omega\ \text{yr})$. The estimated relative uncertainty in the reference resistance including its calibration and instability is 0.15×10^{-6} . Hence, the uncertainty in the ratio $X_R \equiv R/R_{K-90}$ is completely dominated by the uncertainty in R in the as-maintained units.

The individual metal foil resistors forming the sensing resistor R are not perfectly stable under thermal cycling. These resistors will exhibit some time-dependent drift after being cooled from ambient conditions to 273.16 K in a WTP cell. The drift is manifest as an exponential relaxation starting from the original thermal cycle, which presumably is due to a differential expansion strain in the foil. Measurements of the resistance are normally made only after a day or so after the R probe is inserted into the WTP cell. We assign a relative uncertainty of 0.5×10^{-6} to account for the effects of the resistance-relaxation effect.

The general formulation of the Nyquist formula for the mean-squared voltage fluctuations across an arbitrary impedance $Z(f)$ is governed by only the real or dissipative part $\text{Re}\{Z(f)\}$, which is $4kT\ \text{Re}\{Z(f)\}$ in the low-frequency limit (i.e. $f \ll kT/h$) [26]. The resistance is measured at dc only, so any difference between the dc value R_{dc} and $\text{Re}\{Z(f)\}$ results in an error in the inferred value for kT .

Several physical effects need to be considered in evaluating $\Delta Z(f) \equiv \text{Re}\{Z(f)\} - \text{Re}\{Z(0)\}$. First there is the effect of ordinary but small parasitic shunt capacitance C_R and series inductance L_R associated with the resistor. This results in the usual modification of the form $\Delta Z(f) \cong R_{dc}(1 + 2(\tau_{LC}\omega)^2 - (\tau_{RC}\omega)^2)$, where $\tau_{RC} \equiv RC_R$, $\tau_{LC} \equiv L_R C_R$ and $\omega = 2\pi f$. Thus, the leading terms are quadratic in frequency and so would be indistinguishable from the larger quadratic terms governed by the reactances associated with the transmission-line cabling. These types of errors are then of no consequence when the spectral ratio is already being fitted for a quadratic frequency coefficient a_2 . Similar to the above discussion in section 4.1, any losses $\tan(\delta_{RC})$ associated with the small capacitance of the resistor foil's ceramic substrate would produce a linear frequency dependence with a coefficient $a_1 \cong -2\pi\tau_{RC}\tan(\delta_{RC})$, but we estimate this would be smaller by a factor of 10 or more than that already given above. For the frequency dependence of the resistor, we assign a relative uncertainty of 0.1×10^{-6} to account for any departures from pure quadratic behavior in the resistance. Finally, the normal departures from uniform current density, which take place as frequency increases in any conductor, will also produce frequency dependence in the measured resistance. In this case the frequency dependence is governed by the ratio t/δ_s , where t is the thickness of the foil and $\delta_s = (2\rho/\omega\mu)^{-1/2}$

Table 3. Sensing resistance measurement uncertainties.

	$u_r/10^{-6}$
R_{K-90}	0.02
Statistics	0.40
Reference resistor	0.15
Relaxation effects	0.50
Frequency dependence	0.10
Thermoelectric effects	0.10
$u_r(R)$	0.67

is the so-called skin depth. It can be shown [27] that the surface impedance of a thin conducting sheet of resistivity ρ is

$$Z_s = \frac{\rho}{\delta_s} \frac{(1+j)}{\tanh(t(1+j)/2\delta_s)} \cong \frac{2\rho}{t} \left[1 + \frac{2j}{3} \left(\frac{t}{2\delta_s} \right)^2 + \frac{4}{45} \left(\frac{t}{2\delta_s} \right)^4 + O \left(\frac{t}{2\delta_s} \right)^6 \dots \right]. \quad (5)$$

The leading real term in the power series expansion of equation (5) is of fourth order in t/δ_s , which is of second order in frequency. Thus the ac resistance is again modified in the same way as in the previous case, and the quadratic frequency dependence is indistinguishable from the ordinary filtering terms already being accounted for in the fit.

Another origin of finite values for $\Delta Z(f)$ is thermoelectric effects, which give rise to errors in R_{dc} and rapidly diminish with increasing frequency. The effects that are of first order in the Seebeck coefficient are normally canceled by current reversal. There are, however, second-order thermoelectric effects that do not cancel with current reversal but rather add [28]. In order to uncover any possible sign of these second-order effects, we measured our foil resistors at dc and both 30 Hz and 90 Hz ac excitation and found that $\Delta Z(f)$ for the two test frequencies was effectively zero within the uncertainties of the measurements. We account for any remaining undetected presence of these effects with a relative uncertainty component of 0.1×10^{-6} .

Table 3 lists the various uncertainty components for the resistance measurement. The combined uncertainty for the resistance measurement $u(R)$ is the RSS of the individual uncertainty components.

4.3. Water triple point realization

The resistance probe is directly immersed into the thermowell of a standard water triple-point cell. While T_{WTP} is defined in the SI as exactly 273.16 K, we can realize the definition only to within a combined uncertainty $u(T_{WTP})$, which depends on a number of limiting effects. The individual uncertainty components are listed in table 4.

The cell body is a standard design made from borosilicate glass and it contains distilled and de-gassed continental ground water. The pressure head correction is nominally $-0.2\ \text{mK}$ for the cell, but an uncertainty of $0.05\ \text{mK}$ is assigned to the correction due to ambiguities in the effective depth of the sensing resistor originating from the probe design. The

Table 4. Standard uncertainties of the realization of the water triple point temperature.

	$u_r/10^{-6}$
Pressure head correction	0.18
Immersion errors	0.73
Isotopic variation	0.26
Chemical impurities	0.18
Thermal equilibrium	0.18
$u_r(T_{\text{WTP}})$	0.84

temperature as realized in the cell is 273.1598 K, and this value used in the calculations.

The thermowell is filled with ethanol to promote heat transfer along the approximately 30 cm of the immersion column roughly corresponding to the height of the ice mantle. The construction of the probe utilizes a 6.3 mm diameter stainless steel sheath over most of the probe length. The interior consists of two 1.5 mm diameter tubes as grounded shields for each twisted pair of lead wires. Despite this generally conservative design, the probe's immersion characteristics are imperfect, and the probe exhibits immersion errors greater than that of a standard platinum resistance thermometer [29]. A small platinum thermometer is embedded in the interior of the probe housing near the location of the sensing resistor, and this has been used to evaluate the immersion error. A standard uncertainty of 0.2 mK or $0.73 \mu\text{K K}^{-1}$ is assigned to account for immersion errors.

Other uncertainties exist due to the unknown isotopic composition of the water. We assign a 0.07 mK uncertainty for this unknown variation from the defined composition [30]. The concentrations of chemical impurities are likewise unknown, but based on prior experience with cells of similar design, age and construction, we assign a standard uncertainty of 0.05 mK to account for the effects of impurities.

Special provisions have been added in the most recent resistor package designs to facilitate a lower thermal impedance between the package and the inner copper block of the resistor probe. A printed circuit board 0.5 mm thick made from polyamide facilitates mounting of the sensing resistor package to a flat mounting surface on the block. This circuit board accommodates direct contact between the beryllia header and the mounting block through a 'PCB via' and mediated by a thin layer of heat transfer grease. This design helps ensure that the sensing resistor will equilibrate to the proper temperature of the cell. We assign an uncertainty of 0.05 mK associated with any remaining imperfect equilibration of the sensing resistor with the WTP cell.

4.4. QVNS synthesis, input–output coupling and scaling factor

The quantized nature of the voltage pulses, which are the basis for the synthesized waveforms produced by the QVNS, ensures that the uncertainties arising from the QVNS pseudo-noise signal are small. However, there is still some potential for errors, and the most significant error contribution comes from undesired non-quantized current signals, which are associated

with the pulse-bias signals from the digital code generator that biases the Josephson junctions in the QVNS circuit. The two primary concerns are input–output coupling (V_{IO}), which could produce signals on the QVNS voltage leads, and voltage signals produced by bias currents driving the inductance between the junctions in the QVNS circuit. Multiple dc blocks are used on the pulse-bias leads [10] in order to reduce the unwanted signals that reside in the measurement bandwidth. Fortunately, these signals are small enough that they can be eliminated from the pulse waveform without compromising the pulse quantization. These errors are most significant at higher frequencies and have been determined to be less than 2 pV for tones below 650 kHz. Assuming that these inductive signals were combined in quadrature with the Josephson voltage signals, they would contribute about 2×10^{-9} to the relative uncertainty. Note that without the dc blocks, the $\sim 4 \mu\text{H}$ geometric inductance of the Josephson array circuit would produce a 130 pV signal, which in quadrature would generate a quadrature error of $\sim 7 \times 10^{-6}$.

Another effect that can limit measurement uncertainty is variations in the voltage amplitudes of the synthesized harmonic tones for the QVNS waveform due to digitization or 'quantization' noise, which is inherent in the digital-to-analogue generation of the desired waveform signal from the discrete high-frequency QVNS pulses. The software generating the code for the QVNS shapes this digitization noise and moves most of it to the high-frequency end of the spectrum. A third-order modulator algorithm is used to produce the waveforms for this paper, and their amplitudes at 650 kHz deviate from the target voltage by less than 5 parts in 10^7 . Calculated corrections could be applied to remove these exactly calculable variations in the waveform from the measurement [12]. Because this variation does not currently limit the measurement uncertainty, and can be removed in the future, we have not included it in the uncertainty analysis.

4.5. Combined total uncertainty

The total combined standard uncertainty in the measurement of k is calculated as the RSS of the principal uncertainty components. The summary is shown in table 5. The uncertainty for the Planck constant is the recommended CODATA estimate [12]. This determination, as per equation (1), is for the proportionality between k and h , hence, the only SI unit realizations required are for temperature and time. The second is realized from our local timebase f_s . The clock frequencies for the sampling and pulse bias source use a 5 MHz reference that is accurate to a few parts in 10^{15} and is traceable to the NIST primary frequency standard (NIST-F1) and others around the world.

The dominant uncertainty is from the experimental determination of the spectral power ratio, and the dominant component of that uncertainty is from the spectral aberrations discussed in section 4.1.

5. Conclusion

We have determined the Boltzmann constant by use of data derived from the comparison of Johnson noise with quantized

Table 5. Principle standard uncertainty components for the determination of k in equation (1).

Component	Factor or error term	$u_r/10^{-6}$
Spectral power ratio	V_R^2/V_Q^2	12.0
Resistance measurement	X_R	0.67
Temperature realization	T_{WTP}	0.84
Input-output coupling	V_{IO}	0.002
Planck constant	H	0.05
Sampling frequency	f_s	$\ll 0.001$
$u_r(k)$		12.1

voltage noise as synthesized via pulse-biased Josephson arrays. The Johnson noise was derived from a known resistance at a known temperature, and the quantized voltage noise was derived from noise waveforms of calculable spectral density. Measurements were performed with two different reference waveforms constructed from harmonic tones of different amplitudes and tone spacings. The noise power of the harmonic tones of the reference waveforms was matched to the spectral power density of the resistor. The SI kelvin and second are the only two unit realizations required for this determination.

The results are based on two measurement sets taken three months apart and subject to different experimental conditions and different noise synthesis parameters. The only correction required was a simple fitting process to remove remnant quadratic frequency dependence in the ratio spectra. Our data yield $(k - k_{2006})/k_{2006} = +0.6(12.1) \times 10^{-6}$ or $k = 1.380\,651(17) \times 10^{-23} \text{ J K}^{-1}$. The value determined is directly proportional to the Planck constant, for which we use the CODATA 2008 value. The result from our data may be restated as the ratio of the Boltzmann constant to the Planck constant or $k/h = 20.836\,66(25) \text{ GHz K}^{-1}$.

Our estimated uncertainty is dominated by systematic effects that produce aberrations in the ratio spectra and by the random statistical uncertainties achievable given the available volume of data that were accumulated over 116.6 h for each data set. Neither of these contributions are currently thought to represent fundamental limits on this electronic measurement of the Boltzmann constant, and further improvements in the electronics are expected to yield even lower uncertainties than those reported here.

Acknowledgments

The authors thank Charlie Burroughs for chip packaging, Norm Bergren for QVNS fabrication and technical assistance, Anthony Kos for constructing new ADC boards, Sae Woo Nam for creative ideas and years of productive collaboration, Ryan Toonen for early measurements of amplifier non-linearities, Thijs Veening for electronics assembly and Rand Elmquist for providing our traceability to the QHE ohm. They also thank John Martinis for inspiring the QVNS-JNT program and for designing the original electronics, and Carl Williams for support of the NIST JNT/Boltzmann constant program. This work was performed at and supported by the National Institute of Standards and Technology. It is a contribution of the US government that is not subject to US copyright.

References

- [1] Benz S P, Martinis J M, Nam S W, Tew W L and White D R 2002 A new approach to Johnson noise thermometry using a Josephson quantized voltage source for calibration *Proc. TEMPMEKO 2001 (Berlin)* ed B Fellmuth *et al* (Berlin: VDE) pp 37–44
- [2] Tew W L, Benz S P, Dresselhaus P D, Rogalla H, White D R and Labenski J R 2010 Recent progress in noise thermometry at 505 K and 693 K using quantized voltage noise ratio spectra *Int. J. Thermophys.* **31** 1719–38
- [3] White D R and Benz S P 2008 Constraints on a synthetic-noise source for Johnson noise thermometry *Metrologia* **45** 93–101
- [4] White D R, Benz S P, Labenski J R, Nam S W, Qu J, Rogalla H and Tew W L 2008 Measurement time and statistics for a noise thermometer with a synthetic-noise reference *Metrologia* **45** 395–405
- [5] Benz S P, Qu J, Rogalla H, White D R, Dresselhaus P D, Tew W L and Nam S W 2009 Improvements in the NIST Johnson noise thermometry system *IEEE Trans. Instrum. Meas.* **58** 884–90
- [6] Qu J, Benz S P, Rogalla H and White D R 2009 Reduced nonlinearities and improved temperature measurements for the NIST Johnson noise thermometer *Metrologia* **46** 512–4
- [7] Toonen R C and Benz S P 2009 Characterizing the non-linear behavior of single process components with precision multi-tones from a Josephson arbitrary waveform synthesizer *IEEE Trans. Appl. Supercond.* **19** 715–8
- [8] Qu J, Benz S P, Pollarolo A and Rogalla H 2011 Reduced nonlinearities in the NIST Johnson noise thermometry system *IEEE Trans. Instrum. Meas.* at press
- [9] Pollarolo A, Qu J, Rogalla H, Dresselhaus P D and Benz S 2011 Development of a four-channel system for Johnson noise thermometry *IEEE Trans. Instrum. Meas.* at press
- [10] Benz S P, Dresselhaus P D and Burroughs C J 2011 Multitone waveform synthesis with a quantum voltage noise source *IEEE Trans. Appl. Supercond.* at press
- [11] Benz S P, White D R, Qu J, Rogalla H and Tew W L 2009 Electronic measurement of the Boltzmann constant with a quantum-voltage-calibrated Johnson-noise thermometer special issue on the Experimental determination of the Boltzmann constant *C. R. Acad. Sci.* **10** 849–58
- [12] Mohr P J, Taylor B N and Newell D B 2008 CODATA recommended values of the fundamental physical constants: 2006 *Rev. Mod. Phys.* **80** 633–70
- [13] Fischer J *et al* 2008 Preparative steps towards the new definition of the kelvin in terms of the Boltzmann constant *Int. J. Thermophys.* **28** 1753–65
- [14] Mills I M, Mohr P J, Quinn T J, Taylor B N and Williams E R 2005 Redefinition of the kilogram: a decision whose time has come *Metrologia* **42** 71–80
- [15] Johnson J B 1927 Thermal agitation of electricity in conductors *Nature* **119** 50–1
- [16] Nyquist H 1928 Thermal agitation of electric charge in conductors *Phys. Rev.* **32** 110–13
- [17] Brixy H *et al* 1992 *Temperature, Its Measurement and Control in Science and Industry* vol 6, ed J Schooley *et al* (New York: American Institute of Physics) pp 993–6
- [18] White D R *et al* 1996 The status of Johnson noise thermometry *Metrologia* **33** 325–35
- [19] White D R and Zimmermann E 2000 Preamplifier limitations on the accuracy of Johnson noise thermometers *Metrologia* **37** 11–23
- [20] Labenski J R, Tew W L, Nam S W, Benz S P, Dresselhaus P D and Burroughs C J 2007 *IEEE Trans. Instrum. Meas.* **56** 481–5

- [21] Mumby S J and Yuan J 1989 Dielectric properties of FR-4 laminates as a function of thickness and the electrical frequency of the measurement *J. Electron. Mater.* **18** 287–92
- [22] Willink R and White D R 1998 Detection of corruption in Gaussian processes with application to noise thermometry *Metrologia* **35** 787–98
- [23] White D R and Mason R S 2004 An EMI test for Johnson noise thermometry *Proc. TEMPMEKO 2004 (Cavtat-Dubrovnik, Croatia)* (Zagreb: Faculty of Mechanical Engineering and Naval Architecture) ed D Zvizdic *et al* pp 485–90
- [24] Elmquist R E, Jarrett D G, Jones G R, Kraft M E, Shields S H and Dziuba R F 2004 NIST Measurement service for DC standard resistors *NIST Technical Note* 1458, (Washington, DC: US Government Printing Office)
- [25] Taylor B N and Witt T J 1989 New international electrical reference standards based on the Josephson and quantum Hall effects *Metrologia* **26** 47–62
- [26] Weber J 1956 Fluctuation dissipation theorem *Phys. Rev.* **101** 1620–6
- [27] Kennelly A E, Laws F A and Pierce P H 1915 Experimental researches on skin effect in conductors *Trans. Am. Inst. Electr. Eng.* **34** 1953–2018
- [28] Kirby C G M and Laubitz M J 1973 The error due to the Peltier effect in direct-current measurements of resistance *Metrologia* **9** 103–6
- [29] Mangum B W and Furukawa G T 1990 Guidelines for realizing the International Temperature Scale of 1990 (ITS-90) *NIST Technical Note* 1265 (Washington, DC: US Government Printing Office)
- [30] Consultative Committee for Thermometry 2006 *Mise en pratique* for the definition of the kelvin (Sèvres, France: Bureau International des Poids et Mesures)